Research Article Vol. 32, No. 10 / 6 May 2024 / Optics Express 16901
Optics EXPRESS

Tunable polarization control with self-assembled arrays of anisotropic plasmonic coaxial nanocavities

HAIBIN NI,[1,*] AN PING,[1] TONG CAI,[1] BO NI,[1] JIANHUA CHANG,[1] AND ALEXEY V. KRASAVIN[2]

[1]*Jiangsu Provincial Key Laboratory of Meteorological Observation and Information Processing, School of Electronics and Information Engineering, Nanjing University of Information Science and Technology, Nanjing, 210044, China*
[2]*Department of Physics and London Centre for Nanotechnology, King's College London, Strand, London WC2R 2LS, UK*
[*]*nihaibin@nuist.edu.cn*

Abstract: Polarization control with nanostructures having a tunable design and allowing inexpensive large-scale fabrication is important for many nanophotonic applications. For this purpose, we developed and experimentally demonstrated nanostructured plasmonic surfaces based on hexagonal arrays of anisotropic coaxial nanocavities, which can be fabricated by a low-cost self-assembled nanosphere lithography method. Their high polarization sensitivity is achieved by engineering anisotropy of the coaxial nanocavities, while the optical response is enhanced by the excitation of surface plasmon resonances. Particularly, varying the geometrical parameters of the coaxial nanocavities, namely the height and tilt angle of their central core nanoellipsoids, the plasmonic resonance wavelengths as well as the polarization-selective behavior can be individually tuned in the entire visible and near-infrared spectral regions, which makes such nanostructures good candidates for the implementation of polarization-controlled optical switches and polarization-tunable filters. Moreover, the developed nanostructures demonstrate sensitivity up to 1335 nm/RIU in refractive index sensing.

1. Introduction

Surface plasmons are highly-localized electromagnetic excitations that arise from coupling of light with collective oscillations of electrons at the metal/dielectric interfaces [1]. They can be either propagating surface waves at the extended, possibly nanostructured, metallic boundaries (surface plasmon polaritons, SPPs) or localized modes supported by metallic nanoparticles (localized surface plasmons, LSPs). The ability of surface plasmons to confine, control and enhance light at a subwavelength scale together with their high sensitivity to environmental changes provide unique prospects for light manipulation at the nanoscale [2–5], development of highly-integrated photonic integrated circuits [6,7], optoelectronic devices [8,9] and artificial materials with an engineered or greatly enhanced optical response [10–15], together with advances in nonlinear optics [16,17] and chemo-/bio-sensing [18–20].

As plasmonic resonances are highly dependent on the shape of the metallic nanostructures, symmetry breaking of the nanostructure geometry results in pronounced sensitivity of the plasmonic response to the polarization of the incident light. Compared to conventional methods, polarization manipulation with nanostructures provides both polarization and phase control with high spatial resolution. In this respect, extensive efforts have been made to develop various nanostructure designs with polarization-dependent optical behavior, particularly using Fano resonances [21–25]. For example, properly positioned pairs of rectangular nanoholes can be used for polarization-sensitive tunable directional coupling of light to SPPs [26,27], generation of a

#519827 https://doi.org/10.1364/OE.519827
Journal © 2024 Received 24 Jan 2024; revised 4 Apr 2024; accepted 4 Apr 2024; published 23 Apr 2024

Optics EXPRESS

holographic contour [28,29] and control of Airy plasmons [30]. Along with this, a plasmonic filter based on polarization-controlled reproduction of colors was demonstrated with arrays of asymmetric cross-shaped nanoapertures in a thin aluminum film [31]. The double-nanoring pattern can realize polarization-insensitive as well as polarization-sensitive dual-band absorption. A surface plasmon polarization-controlled beam splitter based on slot waveguides and integrated in a plasmonic circuitry was realized for applications in optical signal processing and optical computation [32]. However, most of these devices need to be fabricated using rather expensive lithographic techniques or ion beam milling, which hinders their large-scale manufacturing.

In this paper, we employ a robust and inexpensive self-assembly method based on nanosphere lithography to realize large-scale arrays of anisotropic coaxial plasmonic nanocavities with an engineered plasmonic response and achieve polarization management of the reflected light in both visible and NIR spectral regions. Designing nanocavity surface plasmon resonances supported by the nanocavities provides the means to control absorption efficiency for different polarization states of the incident light over a wide range of incident angles. The contrast in the reflection for orthogonal polarizations is determined by the geometrical parameters of nanoellipsoids producing the core of the coaxial nanocavities and can be easily defined at the fabrication stage. Moreover, by tuning the nanoellipsoid height, tilt angle and semi-axes values it is possible to control not only the far field polarization state, but also the local vectorial distribution of the electromagnetic field. The proposed structure, featuring inexpensive and scalable self-assembly fabrication, can find applications in polarization-sensitive optical switches, spatial light modulators and optical sensing devices.

2. Self-assembly fabrication of anisotropic nanocavity arrays

The arrays of anisotropic plasmonic nanocavities (APNs) were fabricated using a nanosphere lithography method combined with tilted metal deposition. The fabrication process includes four steps (Fig. 1(a)). Firstly, hexagonal polystyrene sphere (PS) arrays ($p = 690$ nm) embedded in a silica gel layer were formed by self-assembly of the spheres upon drying from a water solution with an added silica gel (20 h, 1%vol PS, 0.01%vol silica precursor solution). Secondly, the PS spheres were partially etched by O_2 reactive ion etching (RIE) to form shallow ring gaps between the remaining polystyrene core and the silica gel matrix (not affected by the etching). Thirdly, a silver film was deposited on the etched structures by magnetron sputtering. Adjusting the time of the magnetron sputtering, one can control the vertical base height h of the nanocavities (Fig. 1(b)). Finally, a tilted thermal evaporation was employed for the directional metal deposition to obtain the APNs. During this process asymmetric core structures in a form of nanoellipsoids defining the geometry of the plasmonic nanocavity are formed. The evaporation angle (70°, Fig. 1(a)) defines the nanoellipsoids' tilt angle θ, while the evaporated film thickness and PS etching degree determine their aspect ratio $s = a/b$, where a and b are the nanoellipsoid semi-axes.

Importantly, as a result of the tilted deposition, the nanoellipsoids are oriented in the plane of the sample, producing a hexagonal array of plasmonic coaxial nanocavities with an anisotropic geometry and therefore an anisotropic optical response (Fig. 1(a), (b). Depending on the fabrication conditions, the nanoellipsoids can be either separated from the outer walls of the nanocavity or attached to them by one end. The obtained APN arrays with various geometrical parameters are shown in Fig. 1(c). Particularly, four combinations of magnetron sputtered silver film thicknesses ($h = 50$ nm and $h = 100$ nm) and evaporated film thicknesses (80 nm ($s = 1.37$) and 160 nm ($s = 2$)) are presented. From the top SEM images one can estimate the lengths of the semi-axes and the distances between nanoellipsoids and cavity walls along a semi-axis, e.g. $2a \cdot \sin\theta = 304$ nm, $2b = 235$ nm, $L_1 = 130$ nm and $L_2 = 148$ nm for the top-left structure in Fig. 1(c). As the thermal evaporation time increases, a and L_1 increase, while b and L_2 are kept almost constant, which results in the increase of s. Thus, the geometry parameters h, s, a, b and θ can be continuously tuned during the fabrication process, resulting in the robust control

Optics EXPRESS

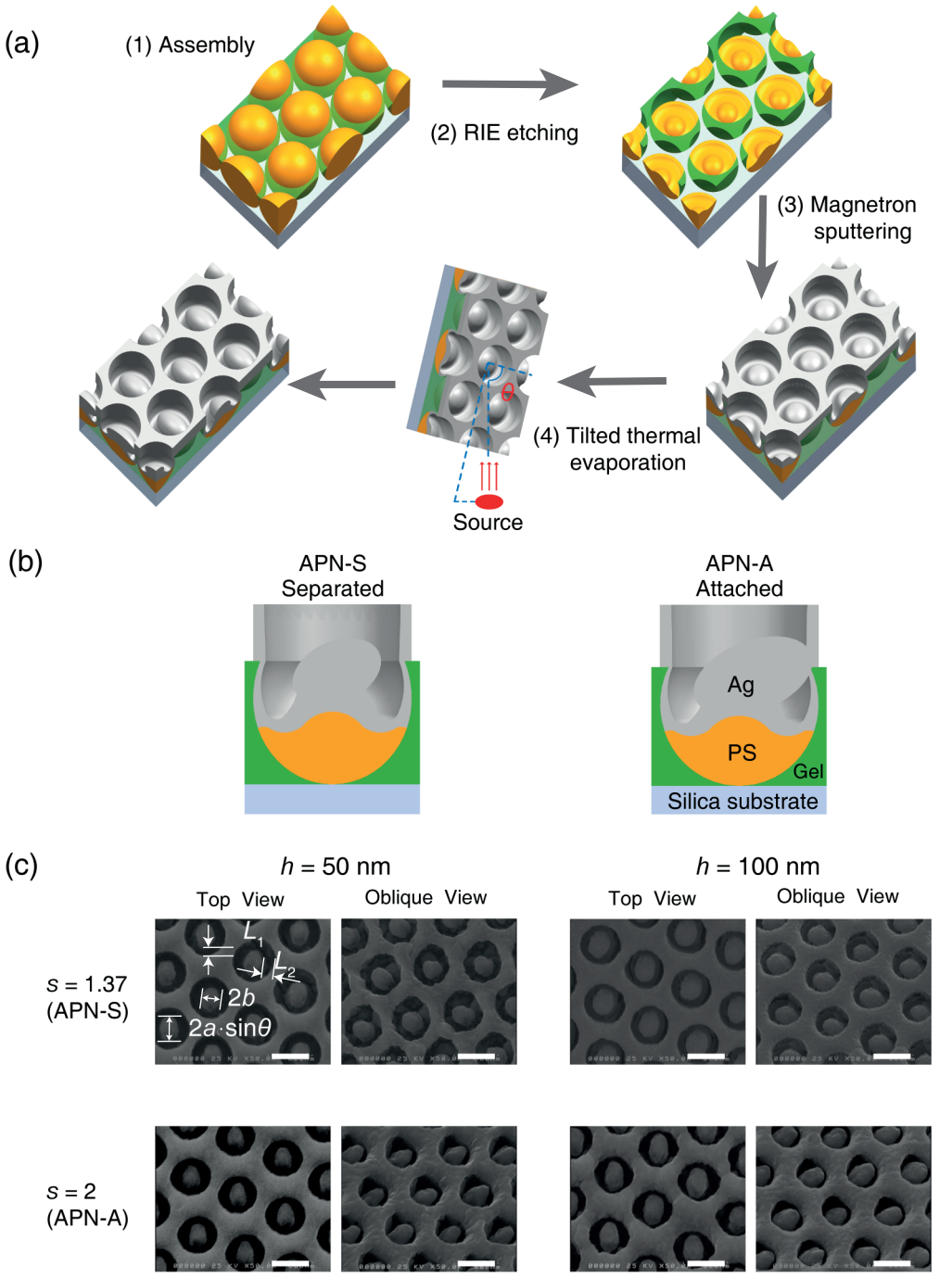

Fig. 1. (a) Fabrication process of the APN arrays: (1) hexagonal PS spheres arrays (period $p = 690$ nm) embedded in a silica gel are formed by self-assembly of the spheres, (2) the PS spheres are etched using RIE, (3) a silver film is deposited by magnetron sputtering, (4) tilted nanoellipsoids are formed at the center of the nanocavity using directional ($\theta = 70°$) evaporation. (b) Cross-sections of the obtained APN designs with separated (APN-S) and attached (APN-A) nanoellipsoids. (c) SEM images of the APN arrays with various geometrical parameters. All scale bars are 500 nm.

Optics EXPRESS

of the polarization-dependent optical response of the nanostructure. The high uniformity of the fabricated samples can be seen in the large-area SEM images presented in Fig. SI-1 of the Supplement 1.

3. Nanostructure operation

3.1. Polarization-sensitive optical response

To understand the polarization-dependent optical response of the nanocavity arrays, numerical simulations of their reflectivity at normal incidence were performed using a finite element method (COMSOL Multiphysics software package). As the optical response largely depends on whether the nanoellipsoids are separated or attached, both cases with characteristic parameters taken from fabrication were numerically simulated, particularly APN-S (separated) and APN-A (attached). In either case the center of the ellipsoid nanoparticle was lifted above the top surface of the magnetron-deposited silver layer (having the height h, Fig. 1(b)) at a distance of 80 nm. The obtained reflection spectra, presented in Fig. 2, show pronounced minima, corresponding to the resonant excitation of plasmonic modes. As a result of the symmetry breaking in the individual nanostructures and the consequent anisotropy of the array, different reflection spectra are observed for the two principal orthogonal polarizations of the incident light ($\varphi = 0°$ and $\varphi = 90°$, defined in Fig. 1(a)).

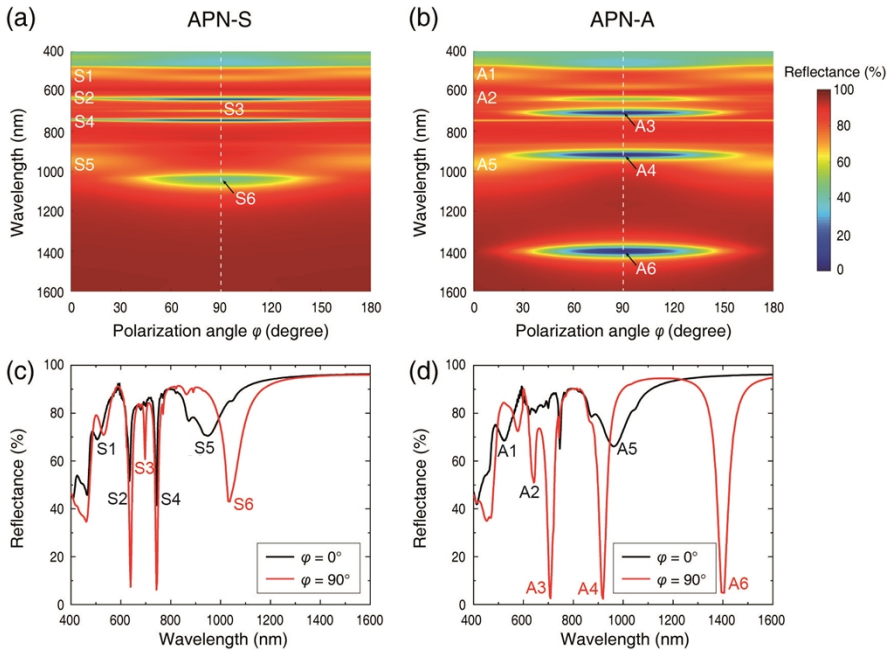

Fig. 2. Numerically simulated normal-incidence reflectance spectra of the coaxial arrays with (a) separated (APN-S, $a = 200$ nm, $b = 120$ nm, $h = 50$ nm, $\theta = 70°$, $s = 1.66$) and (b) attached (APN-A, $a = 240$ nm, $b = 120$ nm, $h = 100$ nm, $\theta = 70°$, $s = 2.33$) core nanoellipsoids. (c), (d) Cross-sections of (a) APN-S and (b) APN-A, respectively, presenting reflectance spectra at $\varphi = 0°$ and 90°.

3.2. Origin of the plasmonic modes

To identify the origin of the excited plasmonic modes related to the reflectivity minima, both the electromagnetic field and current density maps at the resonance wavelengths were analyzed

Optics EXPRESS

(Fig. 3). Particularly, the distribution of the electric field in the gaps between the nanoellipsoids and the nanocavity walls indicates the resonant excitation of nanocavity plasmonic modes unavoidably hybridized with the plasmonic modes of the nanoellipsoid, as can be further observed in the corresponding surface charge distributions. These modes can have predominantly localized (S1 and S5/S6) or coupled/hybrid (to some extent collective, the rest of the modes) nature, which was revealed by simulation of arrays with artificially enlarged periods (see Supplement 1, Fig. SI-2 – 4). In the case of separated nanoellipsoids, high-order nanocavity modes S1, S2 and S4 keep their spectral positions with the change of the polarization angle φ from 0° to 90°, while their excitation magnitudes can be modified (Fig. 2). On the other hand, the spectral position of the nanocavity mode hybridized with the nanoellipsoid dipolar resonances along the short (S5) and the long (S6) nanoellipsoid semi-axes (Fig. 3(a)) significantly depends on the incident polarization. In addition, for the polarization along the nanoellipsoid long semi-axis a localized gap mode appears (S3), confined in the narrowest point of the nanocavity.

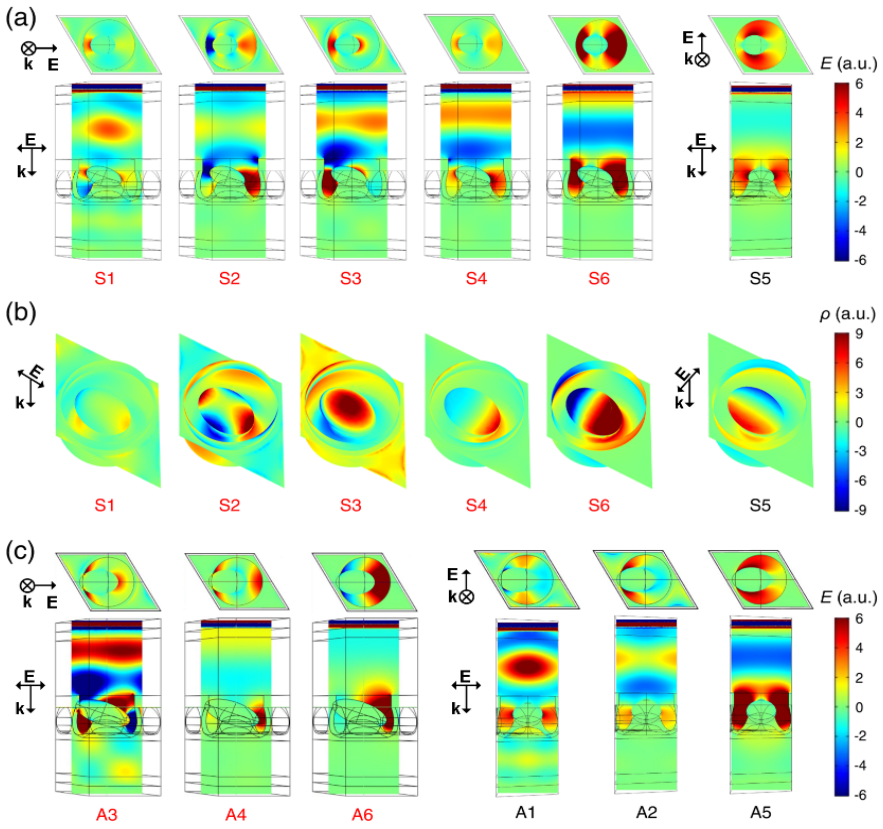

Fig. 3. Numerically simulated distributions of the electric field component collinear with the polarization direction of the incident plane wave, presenting the excitation of resonant plasmonic modes (a) in the case of isolated core nanoellipsoids (APN-S) with the corresponding charge distributions on the metallic surface presented in (b), and (c) in the case of the nanoellipsoids attached to the outer nanocavity wall (APN-A), modelled for the normal incidence and geometrical parameters from Fig. 1. The correspondence of the excited plasmonic resonances to the polarization state of the incident light $\varphi = 0°$ (black curves in Fig. 2) and $\varphi = 90°$ (red curves in Fig. 2) is reflected by the color of the mode labels.

Optics EXPRESS

In the case of nanoellipsoids attached to the cavity walls (case APN-A), as φ changes from 0° to 90°, reflectance dip A1 changes the spectral position from 559 nm to 596 nm, and new modes A3, A4 and A6 appear at 723 nm, 950 nm and 1504 nm, respectively, while mode A5 disappears. Assessing the field map presented in Fig. 3, A5 is the dipolar-type nanoellipsoid mode (an analogue of mode S5), which in this case can be excited only for one polarization across the elliptical nanoparticle. Its counterpart in the orthogonal direction disappeared, as the nanoparticle is merged with the outer nanocavity wall. Examining the field maps of the modes in the APN-A case, one can see that although these modes are strictly speaking not the coaxial nanocavity modes, as the nanocavity now has an interruption produced by the attached nanoellipsoids, they are related and the former can be evolutionarily traced to the latter. Finally, it can be noted that any intermediate polarization of the incident light can be decomposed into two orthogonal components at 0° and 90°, which will result in the simultaneous excitation of both sets of modes with the corresponding magnitudes and phase delays.

3.3. *Influence of geometrical parameters*

In order to demonstrate the possibility of engineering of the optical response of the anisotropic nanocavity arrays via the control of their geometry at the fabrication stage, numerical simulations of their reflectivity as a function of various geometrical parameters were performed (Fig. 4). Taking the attached-nanoparticle APN-A case with $h = 50$ nm, $\theta = 70°$, $a = 280$ nm and $b = 120$ nm as an initial design, each of the above parameters was parametrically swept while the other kept constant, monitoring the reflectivity for both incident polarizations ($\varphi = 0°$ and $\varphi = 90°$). For $\varphi = 90°$, as the values of h and b increase, wavelengths of all plasmonic modes experience a linear red shift. With the increase of θ, the spectral position of mode A3 exhibits a blue shift, while A4 and A6 move to longer wavelengths. It is important to note that there is a characteristic anti-crossing in the modal dispersion at $\theta = \sim 57°$ where it happens a transition between the separated and the attached elliptical nanoparticle cases, which may be a result of hybridization of the nanocavity modes with the localized plasmonic modes appearing in the narrow gap between the nanoellipsoid tip and the wall. With the increase of a, all plasmonic modes experience a red shift. Here, the transition from separated case to attached case accompanied with the mode anti-crossing happens at $a = \sim 250$ nm. For the illumination with $\varphi = 0°$ polarization, the changes of h, θ and a show little influence on the spectral positions of all plasmonic modes. However, as b increases, modes A1, A2, and A5 exhibit significant red shifts, as this is the parameter

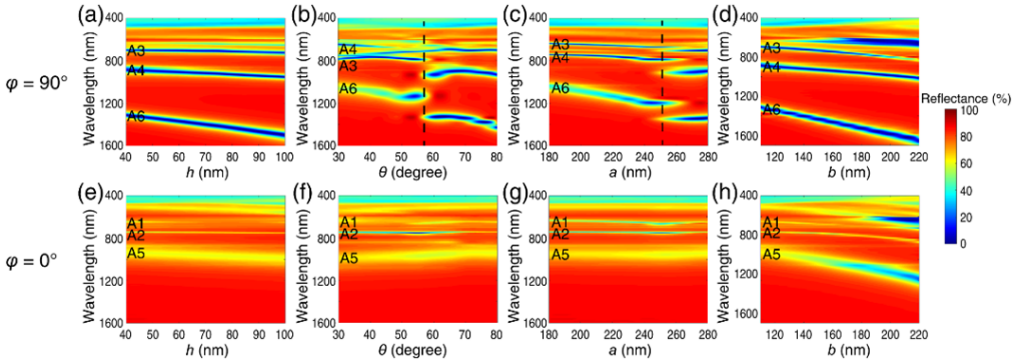

Fig. 4. Numerically simulated reflectance of the APN arrays as a function of the nanocavity parameters: nanoellipsoid base height h (a, e), tilt angle θ (b, f), semi-axes a (c, g) and b (d, h) for two orthogonal polarizations $\varphi = 90°$ (a–d) and $\varphi = 0°$ (e–h). Unless varied, the structural parameters are $h = 50$ nm, $\theta = 70°$, $a = 280$ nm and $b = 120$ nm.

Optics EXPRESS

significantly affecting the width of the nanocavity gap and therefore the optical properties of these modes localized in this region, as can be seen from their field distributions presented in Fig. 3(b).

Overall, one can see that the polarization-sensitive reflectivity happens across the entire visible to near-infrared spectral region and therefore the difference between the reflectivity for $\varphi = 0°$ and $\varphi = 90°$ can be efficiently engineered. By comparing of simulation results for the cases APN-S and APN-A, it is clear that the plasmonic resonances for the case of the attached nanoellipsoid (APN-A) are more sensitive to the polarization variation than that for the case of separated one (APN-S), which can be attributed to a higher level of anisotropy of the structure.

4. Experimental investigation

4.1. Polarization-dependent optical properties

We proceed with experimental investigation of the nanocavity arrays. The experimental setup for measurement of the reflection spectra at normal incidence is presented in Fig. 5(a). A 50 W halogen lamp was used as a broadband optical source. The emitted light was collimated using a pair of lenses before passing through a diaphragm with an aperture, which reduces the size of the light spot to 2 mm. Subsequently, a tunable polarizer (wavelength range 200 – 4000 nm, resolution 2 degrees) was introduced into the optical path to linearly polarize the light. The resulting light beam was incident normally on the sample. The angle in respect to the major anisotropy axes of the sample φ was changed by in-pane rotation of the sample. In order to capture the reflected signal, a half-transparent mirror was positioned in front of the sample. The reflected light is then collected using a 10× objective lens and focused into a multimode optical fiber. Finally, the light signal was analyzed using optical spectrum analyzers (Ocean QE65000 and Ocean NQ 512NIR covering 200 – 1000 nm and 900 – 1700 nm ranges, respectively). Reflection from an Ag film was used as a reference to calculate the sample reflectivity. For measurement of reflection spectra at various angles of incidence α, the half mirror was removed and the lamp together with the lenses, diaphragm and polarizer was placed on a rail positioned at the top of a rotation plate (Fig. 5(b)). The sample was placed on another rotation plate. The rail and sample rotation plate were properly rotated around the same axis to vary the incidence angle with the resolution of 2° and the 10× objective was used to collect the reflected light.

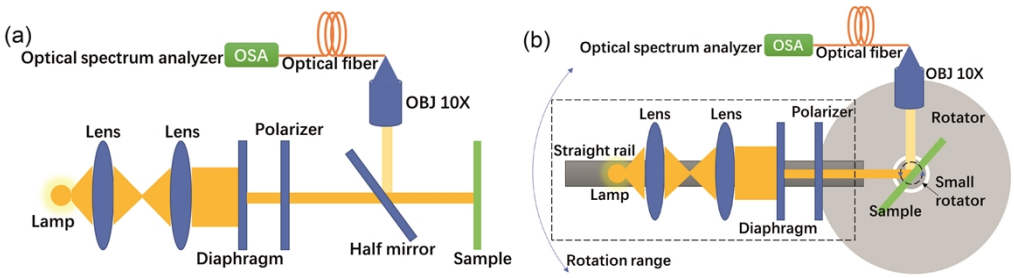

Fig. 5. Experiment setup for measurement of the reflectance spectra at (a) normal and (b) oblique incidence.

Figures 6(a) and 6(b) present the polarization-dependent reflectance spectra of the fabricated separated APN arrays with $s = 1.37$, $h = 50$ nm, $s = 1.37$ and $h = 100$ nm. At $h = 50$ nm, as φ changes from 0° to 90° the excitation of mode S5 gradually decreases, with mode S6 appearing instead, which leads to an effective red shift of the corresponding reflectivity minimum from 1010 nm to 1100 nm with a polarization angle sensitivity (PAS) of ~1.2 nm/deg. When $h = 100$ nm, the PAS increases to ~2.1 nm/deg, which is accompanied, though, with its larger effective FWHM. The measured results are consistent with the simulation counterparts with a slight discrepancy that can be attributed to the difference between the idealized geometry of the models

Optics EXPRESS

and the exact geometry of the measured samples. Similar trends are observed for a larger thickness of the sputtered film $h = 100$ nm.

When the evaporated film thickness is increased to 160 nm, resulting in $s = 2$, the upper side of the nanoellipsoids is almost attached to the cavity wall, which corresponds to the APN-A scenario. In this case, much more pronounced reflectivity changes with the variation of the incident polarization can be observed (Fig. 6(c), (d). With the change of the polarization angle φ, there is an obvious change of the set of the excited modes from (A1, A2, A5) at 0° to (A3, A4, A6) at 90°. The change of the reflection at a given wavelength due to the polarization-sensitive mode excitation reaches many tens of percent, which can be used to realize an optical switch controlled by the polarization of the incident light. Furthermore, as can be seen in Fig. 6(c) and 5(d), the operational wavelength of the switch can be adjusted throughout the visible and near-IR regions by changing only one fabrication parameter h. The measured results ($h = 50$ nm in Fig. 6(c) and $(h) = 100$ nm in Fig. 6(d)) agree quite well with the simulation counterparts, as shown in the line graphs showing the comparison for the two major polarization cases of $\varphi = 0°$ and $\varphi = 90°$, with all the plasmonic resonances could be clearly identified. At the same time, the experimental resonances show substantially larger line widths, which can be explained by structure-to-structure inhomogeneity of the sample and higher losses of the deposited Ag in comparison to the tabulated data used in the simulations. The latter factor can also contribute to the lower experimental reflectance at shorter wavelengths.

4.2. Illumination-dependent optical properties

The dependence of reflectance spectra on the angle of incidence for both $\varphi = 0°$ and $\varphi = 90°$ polarization directions were experimentally measured for the two cases of the base height h (Fig. 7). Due to the in-plane asymmetry of the structure for both polarizations, the measurements were taken in the two principal planes, as illustrated in the top row of Fig. 7(a). While the plasmonic resonances excited with the electric field in the incidence plane containing the long semi-axis ($\varphi = 90°$, Fig. 7(b), (c), (f), (g)) are quite insensitive to the incident angle α, the situation for the orthogonal polarization is quite different. Mode S5 corresponding to the dipolar excitation along the short semi-axis of the nanoellipsoid ($\varphi = 90°$) experiences a substantial spectral shift with the change of the incidence angle in both incidence planes (Fig. 7(d), (f), (h), (i)) with angular sensitivities of 2.9 nm/deg (d), 4.5 nm/deg (e) for $h = 50$ nm and 1.5 nm/deg (h), 2.2 nm/deg (i) for $h = 100$ nm.

4.3. Refractive index sensing

The potential of the APN arrays for sensing of the refractive index (RI) of the environment was estimated using numerical simulations (Fig. 8). As the RI increases, modes A3, A4 and A6 experience a linear red shift with the sensitivities of 670 nm/RIU, 898 nm/RIU and 1335 nm/RIU, respectively. In addition, the modes have spatially different positions of electric field enhancement in the cavity, which makes it possible to independently detect RI changes in different areas at the same time. Particularly, the cavity space can be divided into three regions: 1, 2 and 3 (Fig. 8(b)). The evolution of the spectral positions and the width of the resonances corresponding to modes A3, A4 and A6 with the RI change in these regions is shown in Fig. 8(c)–(e). As the RI in region 1 increases, A3, A4 and A6 experience a linear red shift, with RISs of 383 nm/RIU, 500 nm/RIU and 916 nm/RIU, respectively. As the RI in region 2 increases, modes A4 and A6 experience a linear red shift, with RISs of 216 nm/RIU and 550 nm/RIU, while the spectral position of A3 remains constant. For the RI increase in region 3, mode A4 shows a RIS of 250 nm/RIU, while the spectral position of mode A6 remains constant and mode A3 disappears. The observed levels of sensitivity are typical for the sensors using individual localized resonances [33].

Optics EXPRESS

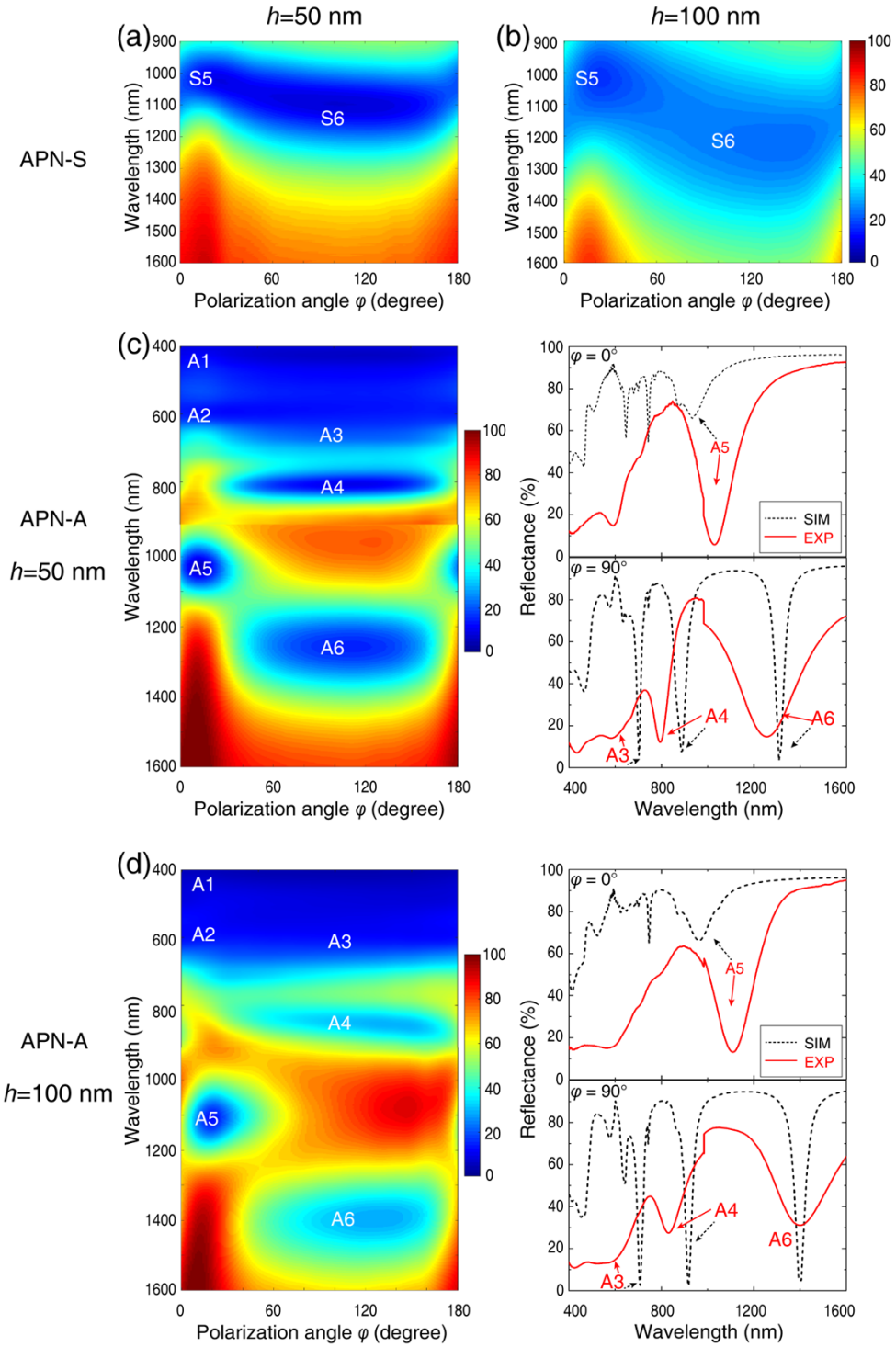

Fig. 6. Experimentally measured reflectance of the separated (a, b) and almost attached (c, d) APN arrays as a function of polarization of the incident light for APNs with a large aspect ratio ($s = 2$) for $h = 50$ nm (a, c) and $h = 100$ nm (b, d). The measurements were performed using visible (400 – 1000 nm) and NIR (1000 – 1600 nm) spectrometers.

Optics EXPRESS

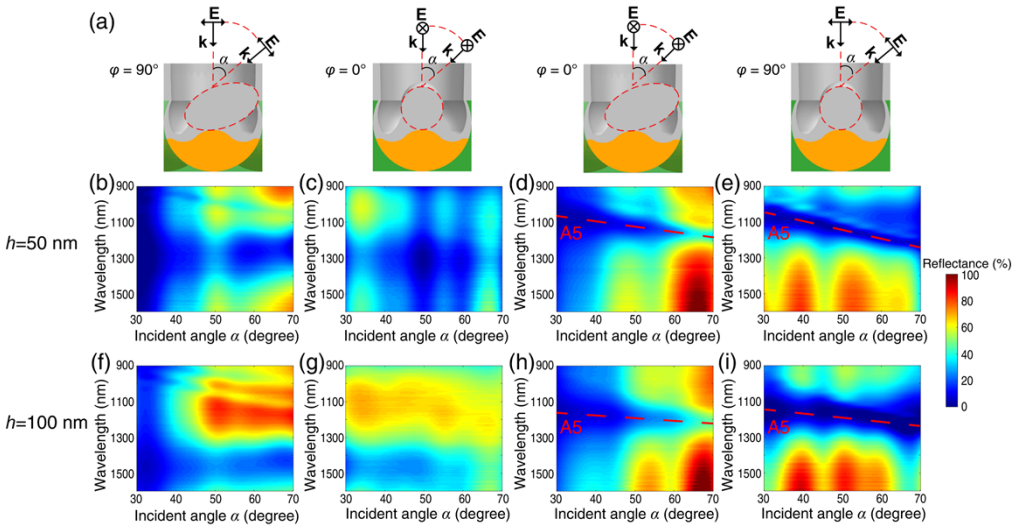

Fig. 7. Experimentally measured reflectance of the almost attached APN arrays (with the same parameters as in Fig. 6(d)) as a function of the incidence angle for four principal combinations of the plane of incidence (containing either long or short semi-axes of the nano-ellipsoid) and the incident light polarization.

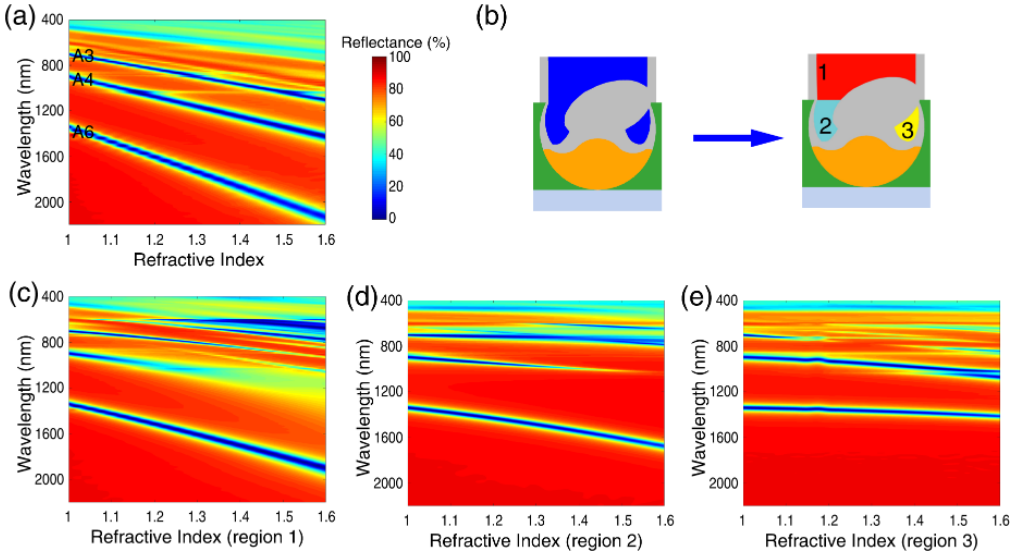

Fig. 8. Numerically simulated reflectance of the ANP-A arrays (with the same parameters as in Fig. 5(d)) at normal incidence and $\varphi = 90°$ polarization as a function of (a) uniform change of the RI of the environment and (c – e) RI change in three nanocavity regions shown in (b).

5. Conclusion

We present a low-cost self-assembly method based on nanosphere lithography for fabrication of large-area arrays of plasmonic nanocavities featuring an anisotropic optical response. The arrays support plethora of hybridized plasmonic modes related to the nanoellipsoid nanocavity

Optics EXPRESS

core and the coaxial nanocavity itself, which due to the in-plane anisotropy of the structure lead to a pronounced polarization-sensitive behavior of the arrays. The modes can be individually tuned by changing the geometrical parameters of the nanoellipsoids at the fabrication stage. The optical response of the arrays is sensitive to the incident angle when the polarization direction is along the short semi-axis of the core nanoellipsoids. In addition, simulation results show that the arrays offer sensitivity to the refractive index of the surroundings as high as 1335 nm/RIU. Furthermore, it is possible to simultaneously and independently detect RI changes in various regions of the cavity by monitoring spectral shifts of the plasmonic modes. Such optical response makes asymmetric nanocavity arrays to be prospective building elements for integrated photonic devices targeting a variety of applications, including polarization-controlled optical switches, spatial light modulators and RI sensors.

Funding. National Natural Science Foundation of China (61605082, 61875089); Natural Science Foundation of Jiangsu Province (BE2016756, BK20160969); Priority Academic Program Development of Jiangsu Higher Education Institutions; China Postdoctoral Science Foundation (2017M611654); Open Research Fund of State Key Laboratory of Digital Medical Engineering.

Acknowledgements. H.N. would like to thank Dr. Yunlu Jiang for the assistance in fabrication of the samples.

Disclosures. The authors declare no conflicts of interest.

Data availability. Data underlying the results presented in this paper are not publicly available at this time but may be obtained from the authors upon reasonable request.

Supplemental document. See Supplement 1 for supporting content.

References

1. S. A. Maier, *Plasmonics: fundamentals and applications* (Springer, 2007), Vol. 1.
2. H. Lee, Z. Liu, Y. Xiong, *et al.*, "Development of optical hyperlens for imaging below the diffraction limit," Opt. Express **15**(24), 15886–15891 (2007).
3. J. Li, A. V. Krasavin, L. Webster, *et al.*, "Spectral variation of fluorescence lifetime near single metal nanoparticles," Sci. Rep. **6**(1), 21349 (2016).
4. T. Kosako, Y. Kadoya, and H. F. Hofmann, "Directional control of light by a nano-optical Yagi–Uda antenna," Nat. Photonics **4**(5), 312–315 (2010).
5. P. R. Wiecha, L. J. Black, Y. Wang, *et al.*, "Polarization conversion in plasmonic nanoantennas for metasurfaces using structural asymmetry and mode hybridization," Sci. Rep. **7**(1), 40906 (2017).
6. Y. Fang and M. Sun, "Nanoplasmonic waveguides: towards applications in integrated nanophotonic circuits," Light: Sci. Appl. **4**(6), e294 (2015).
7. A. V. Krasavin and A. V. Zayats, "Benchmarking system-level performance of passive and active plasmonic components: integrated circuit approach," Proc. IEEE **104**(12), 2338–2348 (2016).
8. D. Y. Fedyanin, A. V. Krasavin, A. V. Arsenin, *et al.*, "Lasing at the nanoscale: coherent emission of surface plasmons by an electrically driven nanolaser," Nanophotonics **9**(12), 3965–3975 (2020).
9. X. Zhang, Q. Xu, L. Xia, *et al.*, "Terahertz surface plasmonic waves: a review," Adv. Photonics **2**(01), 1 (2020).
10. A. Poddubny, I. Iorsh, P. Belov, *et al.*, "Hyperbolic metamaterials," Nat. Photonics **7**(12), 948–957 (2013).
11. N. Yu and F. Capasso, "Flat optics with designer metasurfaces," Nat. Mater. **13**(2), 139–150 (2014).
12. P. Wang, A. V. Krasavin, F. N. Viscomi, *et al.*, "Metaparticles: Dressing Nano-Objects with a Hyperbolic Coating," Laser Photonics Rev. **12**(11), 1800179 (2018).
13. S. Xiao, V. P. Drachev, A. V. Kildishev, *et al.*, "Loss-free and active optical negative-index metamaterials," Nature **466**(7307), 735–738 (2010).
14. D. Vestler, I. Shishkin, E. Gurvitz, *et al.*, "Circular dichroism enhancement in plasmonic nanorod metamaterials," Opt. Express **26**(14), 17841–17848 (2018).
15. S. K. Verma and S. K. Srivastava, "Plasmon mediated extra-ordinary optical transmission through an apertureless plasmonic metagrating," Appl. Phys. Lett. **122**(17), 1 (2023).
16. J. Butet, P.-F. Brevet, and O. J. Martin, "Optical second harmonic generation in plasmonic nanostructures: from fundamental principles to advanced applications," ACS Nano **9**(11), 10545–10562 (2015).
17. G. A. Wurtz, R. Pollard, W. Hendren, *et al.*, "Designed ultrafast optical nonlinearity in a plasmonic nanorod metamaterial enhanced by nonlocality," Nat. Nanotechnol. **6**(2), 107–111 (2011).
18. K. Saha, S. S. Agasti, C. Kim, *et al.*, "Gold nanoparticles in chemical and biological sensing," Chem. Rev. **112**(5), 2739–2779 (2012).
19. S.-Y. Ding, J. Yi, J.-F. Li, *et al.*, "Nanostructure-based plasmon-enhanced Raman spectroscopy for surface analysis of materials," Nat. Rev. Mater. **1**(6), 16021 (2016).
20. A. V. Kabashin, P. Evans, S. Pastkovsky, *et al.*, "Plasmonic nanorod metamaterials for biosensing," Nat. Mater. **8**(11), 867–871 (2009).

Optics EXPRESS

21. A. Lopez-Ortega, M. Zapata-Herrera, N. Maccaferri, *et al.*, "Enhanced magnetic modulation of light polarization exploiting hybridization with multipolar dark plasmons in magnetoplasmonic nanocavities," Light: Sci. Appl. **9**(1), 49 (2020).
22. U. Guler and R. Turan, "Effect of particle properties and light polarization on the plasmonic resonances in metallic nanoparticles," Opt. Express **18**(16), 17322–17338 (2010).
23. B. Luk'yanchuk, N. I. Zheludev, S. A. Maier, *et al.*, "The Fano resonance in plasmonic nanostructures and metamaterials," Nat. Mater. **9**(9), 707–715 (2010).
24. S. K. Verma and S. K. Srivastava, "Experimental demonstration of a Fano resonant hybrid plasmonic metasurface absorber for the O and E bands of the optical communication window," J. Opt. Soc. Am. B **41**(2), 1 (2024).
25. B. Hopkins, A. N. Poddubny, A. E. Miroshnichenko, *et al.*, "Revisiting the physics of Fano resonances for nanoparticle oligomers," Phys. Rev. A **88**(5), 1 (2013).
26. L. Wang, J. Lv, J. Su, *et al.*, "A metasurface for polarization-controlled-phase directional coupling of surface plasmon polaritons," Opt. Mater. **110**, 110469 (2020).
27. J. Lin, J. B. Mueller, Q. Wang, *et al.*, "Polarization-controlled tunable directional coupling of surface plasmon polaritons," Science **340**(6130), 331–334 (2013).
28. J. Chen, T. Li, S. Wang, *et al.*, "Multiplexed holograms by surface plasmon propagation and polarized scattering," Nano Lett. **17**(8), 5051–5055 (2017).
29. Q. Xu, X. Zhang, Y. Xu, *et al.*, "Polarization-controlled surface plasmon holography," Laser Photonics Rev. **11**(1), 1600212 (2017).
30. X. Yin, L. Chen, and X. Li, "Polarization-controlled generation of Airy plasmons," Opt. Express **26**(18), 23251–23264 (2018).
31. Z. Li, A. W. Clark, and J. M. Cooper, "Dual color plasmonic pixels create a polarization controlled nano color palette," ACS Nano **10**(1), 492–498 (2016).
32. M. H. El Sherif, O. S. Ahmed, M. H. Bakr, *et al.*, "Polarization-controlled excitation of multilevel plasmonic nano-circuits using single silicon nanowire," Opt. Express **20**(11), 12473–12486 (2012).
33. K. M. Mayer and J. H. Hafner, "Localized surface plasmon resonance sensors," Chem. Rev. **111**(6), 3828–3857 (2011).